Research Article | Vol. 11, No. 10 / 1 Oct 2021 / Optical Materials Express 3455
Optical Materials EXPRESS

Robust organic functional materials by thermally doping with metal oxide

Bin Wei,[1,2] Yuxuan Fan,[1] Ahui Sun,[2] Kangping Liu,[2] Shuzhe Li,[1] Weixia Lan,[2] Yingjie Liao,[2] Yang Lin,[2,4] and Wai-Yeung Wong[3,5]

[1]*Microelectronic R&D Center, School of Mechanical and Electronic Engineering and Automation, Shanghai University, Shanghai, 200072, China*
[2]*School of Mechatronic Engineering and Automation, Key Laboratory of Advanced Display and System Applications, Ministry of Education, Shanghai University, Shanghai 200072, China*
[3]*Institute of Molecular Functional Materials and Department of Applied Biologyand Chemical Technology, The Hong Kong Polytechnic University, Hung Hom, Kowloon, Hong Kong, China*
[4]*ylin@i.shu.edu.cn*
[5]*wai-yeung.wong@polyu.edu.hk*

Abstract: We have investigated the failure mechanism of organic functional materials and organic light-emitting diodes (OLEDs) by annealing at high temperatures. We found that N,N'-bis(naphthalen-1-yl)-N,N'-bis(phenyl)-benzidine (NPB) doped molybdenum oxide and 1,3,5-tri[(3-pyridyl)-phen-3-yl]benzene doped cesium carbonate can enhance the thermal stability significantly. The former composite film reveals the ions of NPB, as observed by X-ray photoelectron spectroscopy (XPS), the formation of which shows that NPB receives the electron that Mo loses. Meanwhile, it is stable for the binding energy of the element in the latter composite film from the XPS image. Through the research of carrier-only cells, the observation indicates that the thermal stability of the doped cell is better than that of the undoped cell at high temperatures. The current efficiency of the doped device is only reduced by 12% after annealing at 80°C; meanwhile the lifetime reaching 208 h is the longest among that of the devices. Simultaneously, the undoped device represents a larger decline even of about 30% with the lifetime reaching just 40 h. We assumed that the enhanced heat-resisting properties of organic materials by inorganic doping might be attributed to the decrease of energy barrier and the reduction of the interface charge accumulation phenomenon caused by high temperature. Inorganic doping paves an alternative way to substitute for synthesizing expensive functional materials with high glass transition temperature.

© 2021 Optical Society of America under the terms of the OSA Open Access Publishing Agreement

1. Introduction

Continuous development and application have been made on high-efficiency organic semiconductor electroluminescent devices, which have begun to be commercialized [1–3]. However, the thermal stability of organic light-emitting diodes (OLEDs) plays a vital role in practical applications. Heat-induced degradation mechanism of devices can be ascribed to the heat decomposition and/or crystallization of organic material, leading to the cracked molecular structure or destroyed host–guest transfer mechanism [4].

The thermal stability of OLED is closely related to the glass transition temperature (Tg) of organic functional layers used in device. With the increase in the current density, the temperature within organic materials may be close to its Tg, leading to the crystallization of organic materials. Therefore, the thermal-stability compound can effectively prevent the efficiency roll-off of the device.

To obtain good thermal stability, we deliberately studied how to thermally dope low T_g organic materials with inorganic substances. We explore the photophysical properties of the

#437768 https://doi.org/10.1364/OME.437768
Journal © 2021 Received 15 Jul 2021; revised 17 Aug 2021; accepted 27 Aug 2021; published 15 Sep 2021

© 2021 Optica Publishing Group under the terms of the Open Access Publishing Agreement. Users may use, reuse, and build upon the article, or use the article for text or data mining, so long as such uses are for non-commercial purposes and appropriate attribution is maintained. All other rights are reserved.

Optical Materials EXPRESS

N,N'-bis(naphthalen-1-yl)-N,N'-bis(phenyl)-benzidine (NPB) film (hole transport material) and its composite film, respectively. Among them, the NPB whose T_g is 98 °C is a hole transport material commonly utilized in OLED [5]. Its highest occupied molecular orbital (HOMO) and lowest unoccupied molecular orbital (LUMO) are -5.5 and -2.5 eV, respectively, with the mobility reaching 5.1×10^{-4} $cm^2V^{-1}s^{-1}$. For the sake of exploring the influence of doping on the thermal resistance of the device, it is necessary to deeply elaborate the photophysical and electrical properties of the film after high temperature annealing, and to compare the device performance before and after doping.

The main factors affecting the thermal stability of OLEDs are the material and device structure in high-temperature environments [6–9]. In terms of materials, most organic materials currently possess a low T_g, meanwhile high temperatures will crystallize some organic low-T_g functional materials, destroying the performance of the organic material itself and causing charge carrier imbalance inside the device. Simultaneously, the surface morphology of the organic functional layer will be destroyed [10]. Therefore, it is effective for the application of organic materials with higher T_g as the functional layer to achieve the stability of OLEDs at high temperature [11,12]. In addition to applying high T_g organic materials, thermal doping of inorganic oxide to replace the conventional materials is also a better alternative. Inorganic functional materials are not easily affected by external factors such as water and oxygen. Compared with organic materials, inorganic functional materials have a higher melting point and excellent high-temperature stability. The reasons why inorganic materials possess better electron transport characteristics are that they can promote charge carrier injection and transport balance, decrease charge accumulation at the interface of the functional layer, effectively reduce heat generation, and improve device performance. Hence, doping organic material systems with a diverse class of inorganic materials is of great significance to improving the thermal stability of OLEDs.

According to the previous reports [13–15], doping with inorganic materials will improve the heat-resisting properties of the device to a certain extent. Therefore, we mainly investigated the failure mechanism of organic thin films and devices at high temperature and proposed an optimization scheme for low-T_g organic thin films to improve their thermal stability. Here, the main application of utilizing X-ray photoelectron spectroscopy (XPS) is to determine the binding energy of electrons to identify the chemical properties and analysis composition of the sample surface with the purpose of further exploring the mechanism at high temperature. Finally, we studied the effect of high temperature on the performance and lifetime of OLEDs [16,17].

2. Experimental

The devices were fabricated by conventional vacuum deposition of the organic layer and cathode onto an indium-tin-oxide (ITO, 15 Ω, 150 nm) coated glass substrate under a base pressure lower than 5.0×10^{-5} mbar. Glass and ITO substrates were cleaned using detergent, de-ionized water, acetone, and isopropanol. Immediately prior to loading into a custom-made high vacuum thermal evaporation chamber, the substrates were exposed to a UV-ozone environment for 10 min. Then, organic layers and a metal cathode layer were evaporated successively using a shadow mask.

The NPB was employed as hole transport layer (HTL). The 4,4',4"-tris(carbazol-9-yl) triphenylamine (TCTA) was used as the blocking layer between the HTL and the light-emitting layer. Here, the 5,6,11,12-tetraphenylnaphthacene (rubrene) was exploited as the light-emitting guest material, and the tris(8-hydroxyquinolinato)aluminum (Alq_3) was used as the light-emitting host. After the light-emitting layer, we continued to evaporate 20 nm Alq_3 to prevent from the Cesium ion as the HTL for subsequent optimization of the devices. The 1,3,5-tri[(3-pyridyl)-phen-3-yl]benzene (TmPyPB) was used as an electron transport layer (ETL). Due to its wider bandgap, TmPyPB works effectively for carrier transport and also functions as the wide bandgap host in mixed OLED emission layers. The lithium fluoride (LiF) and aluminum (Al) were used as the electron injection layer (EIL) and cathode, respectively. Additionally, the NPB doped with molybdenum

Optical Materials EXPRESS

oxide (MoO_3) serves as a hole injection and HTL for the optimization of the NPB layer. However, for OLEDs, this may also cause the problem that the diffusion of impurity metal ions doped into the light-emitting layer leads to exciton quenching [18] and excessive hole injection, which further reduces the efficiency of the device. In order to prevent the exciton quenching caused by the diffusion of metal ions, it is necessary to insert a blocking layer TCTA between the HTL and the light emitting layer. The TCTA, whose T_g is 150°C, is an organic barrier material with fine thermal stability. By applying TmPyPB doped with cesium carbonate (Cs_2CO_3) as the ETL material, it is also pivotal to insert a layer of high stability transport layer material Alq_3 between the light-emitting layer and the ETL. All of the organic layers and the Al cathode were deposited without exposure to the atmosphere. The deposition rates for the organic materials and Al were typically 1.0 and 5.0 Å s^{-1}, respectively. For the doped layer, two different sensors were used to monitor the deposition rates of both the dopant and the host materials.

The device active area, which was defined by the overlap between the electrodes, was 2×2 mm^2 in all cases. The device structures and the corresponding schematic energy band diagram are shown in Fig. 1(s) (a) and (b), and the chemical structures of the compounds used in the OLEDs are illustrated in Fig. 1(c). The structure design of the Devices A and B are as follows.

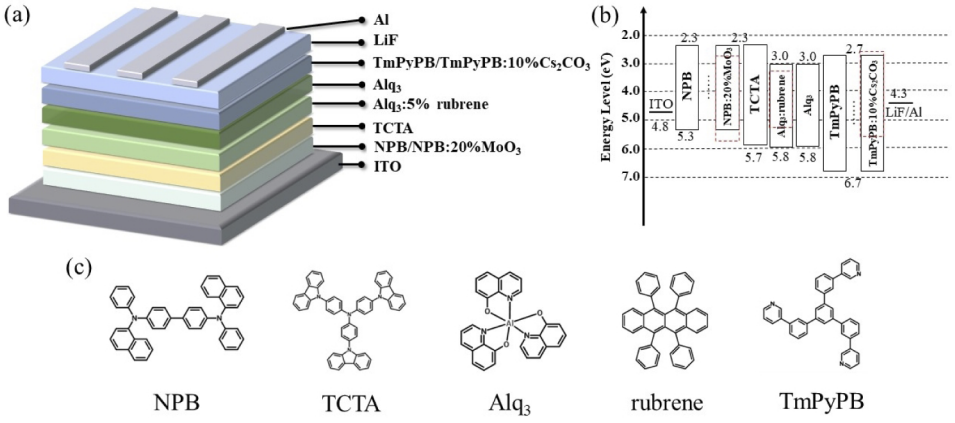

Fig. 1. (a) The device structure for the OLED with NPB or MoO_3-doped NPB and (b) the corresponding schematic energy level diagram for the materials. (c) Chemical structures of the compounds used in the OLEDs.

Device A: ITO/NPB (30 nm)/TCTA (20 nm)/Alq_3: 5 vol% rubrene (20 nm)/Alq3 (20 nm)/TmPyPB (30 nm)/LiF (0.5 nm)/Al (100 nm).

Device B: ITO/NPB: 20 vol% MoO_3 (30 nm)/TCTA (20 nm)/Alq_3: 5 vol% rubrene (20 nm)/Alq3 (20 nm)/TmPyPB: 10 vol% Cs_2CO_3 (30 nm)/LiF (0.5 nm)/Al (100 nm).

The morphology of the film was characterized by the Bruker atomic force microscope (Atomic Force Microscope, AFM). UV–vis absorption spectra were measured with an ultraviolet–visible–near infrared spectrophotometer (UV–2501PC, Shimadu). Photoluminescence characteristics was measured on a single-photon counter from Edinburgh Instruments FLSP920. The binding energy of the elements was measured by Thermo Scientific K-Alpha's X-ray photoelectron spectrometer. The PL emission quantum yield (PLQY) was measured at room temperature in dichloromethane solution. Raman spectra were collected on a Raman spectrometer equipped with a 532 nm laser excitation.

The lifetime of the OLED device was measured by the OLED aging tester. The luminance of the OLED device was controlled by a constant current source, and then the photosensitive detector was fixed on the light-emitting point of the device. After encapsulation, the device was placed on the annealing table for annealing at different temperatures. To achieve the contrast

Optical Materials EXPRESS

after annealing at different temperatures, the initial luminance for tested devices was fixed at 1000 cd m^{-2}.

3. Results and discussion

3.1. Photophysical properties of MoO_x-doped organic functional films

After the identified annealing time, the roughness of the NPB film was measured at the four temperatures, as shown in Fig. 2, which is about 0.462, 1.37, 0.504, and 0.496 nm, respectively. The comparative data depicted that the roughness of the NPB film was 1.37 nm with obvious transformation at 80°C, while the film roughness remained low at the other temperatures. The T_g of NPB is 98°C [19,20], but the morphological change at this time is very similar to the characteristics of glass transition. This is because the glass transition of organic materials is a second-order transition process, which usually occurs in a considerable temperature range, rather than a sudden transition. Meanwhile the NPB film is heated in the air, and the moisture in the air helps the NPB film crystallize [21]. Although the surface roughness of the NPB film is relatively low when the temperature rises to 150 °C, the film has begun to melt and disappear at this time. Only a relatively flat area is selected during the test. In addition, we have also studied the transformation of TmPyPB and its composite film at different high temperature, which was utilized as the ETL of the final device. The process is also the same as above. Under the same annealing time, four annealing temperatures are set at 27, 50, 80 and 100 °C, respectively. As demonstrated in Fig. S1, the roughness of the TmPyPB film after annealing temperature of 27, 50, 80, and 100°C was 0.526, 0.937, 0.519, and 0.544 nm, respectively. The comparative data indicated that the roughness of the TmPyPB film exhibited a significant change under the annealing condition of 50°C. Meanwhile the roughness was 0.937 nm and the roughness of the film remained relatively unchanged at other temperatures. The TmPyPB film surface gradually forms crystallites and the aggregation of TmPyPB molecules leads to a substantial increase in the surface roughness of the film. When the temperature exceeds T_g, the TmPyPB film begins to crystallize and the film becomes smoother.

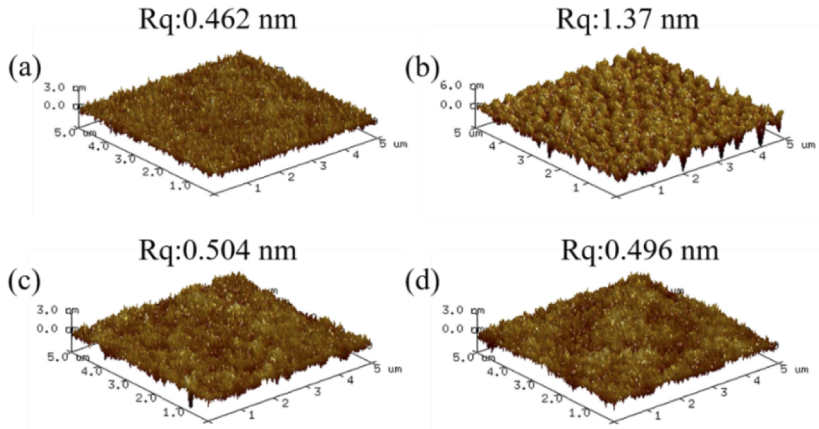

Fig. 2. The morphology of NPB film annealed at different temperatures for 30 min. (a) 27°C; (b) 80°C; (c) 100°C; (d) 150°C.

As shown in Fig. S2, by comparing with the Raman spectrum of NPB crystal [22], it is found that the position of the main peak of the NPB film is very consistent with the position of the main peak of the NPB crystal. Therefore, it can be concluded that after annealing the NPB film at 80 and 100°C in air, there is a crystallization phenomenon in the NPB film.

Optical Materials EXPRESS

The film morphology of the composite film is depicted in Fig. 3 when the film is annealed at different temperatures for 30 min. It could be revealed from the chart that the doped composite film has the film roughness of 0.72, 0.71, 0.72, and 0.68 nm, respectively, annealed at different temperature. The film surface roughness has not changed significantly and is very flat. Meanwhile, the surface morphology of the Cs_2CO_3-doped TmPyPB composite film was investigated by AFM. As illustrated in Fig. S3, the film with TmPyPB: 10 vol% Cs_2CO_3 was annealed at different temperatures for 30 min. It can be clarified from the figure that the morphology of the film remains very smooth. It did not show significant movements after high temperature treatment, forming no crystallite aggregates at 50 °C. It also suggests that Cs_2CO_3 plays a significant role in disturbing the molecular arrangement and preventing the crystallization of TmPyPB.

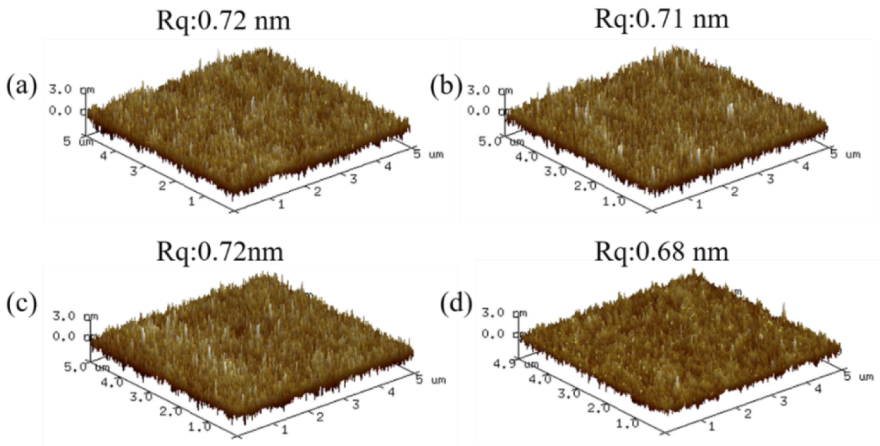

Fig. 3. The morphology of NPB: 20 vol% MoO_3 film annealed at different temperatures for 30 min. (a) 27℃;(b) 80℃(c) 100℃(d) 150℃.

To further discuss the *p*-type doping process of NPB doped with MoO_3, we probed the chemical state of Mo in NPB by the XPS. Moreover, a 100 nm film with NPB: 20 vol% MoO_3 was vapor-deposited on the silicon substrate to avoid that the signal peak intensity of the silicon substrate is too high and the low-intensity signal peaks in the film are not clear. After the evaporation was completed, the film sample was placed on the annealing table and annealed at a high temperature in the air. The annealing temperature is set to 27, 100, and 150 °C, respectively. The test results are presented in Fig. 4.

Compared with the unannealed film, the binding energy of each element transfers to a lower binding energy as a whole after annealing. The binding energy of C 1s and N 1s orbitals decreases, and the element gets electrons. This is because the part of the electrons on the Mo element is transferred to the NPB molecule, forming ions of NPB. For the Mo element, its binding energy shifts to the low field direction, which may be caused by the interaction between the Mo and NPB. To further analyze the influence of high temperature on the composite film, we utilized Gauss/Lorentz mixture function fitting analysis technology to perform peak fitting of the 3d spectra of Mo to obtain different Gaussian peaks after different temperature treatments, where A, B, and C respectively represent Mo $3d_{3/2}$ energy level under Mo^{+6}, Mo^{+5}, and Mo^{+4}, while A', B', and C' represent Mo $3d_{5/2}$ energy level under Mo^{+6}, Mo^{+5}, and Mo^{+4}, respectively, as depicted in Fig. S4. Figure S4(a) shows the Mo 3d orbital analysis of NPB: 20 vol% MoO_3 film at room temperature. The charts reveal that there are multiple valence states of Mo in the composite film. Because the ratio of Mo: O in the film does not meet the stoichiometric ratio of crystalline MoO_3 when OLEDs are prepared by vacuum evaporation method, there are multiple Mo elements in the film [23]. However, this result is closely related to the thickness of the MoO_3

Optical Materials EXPRESS

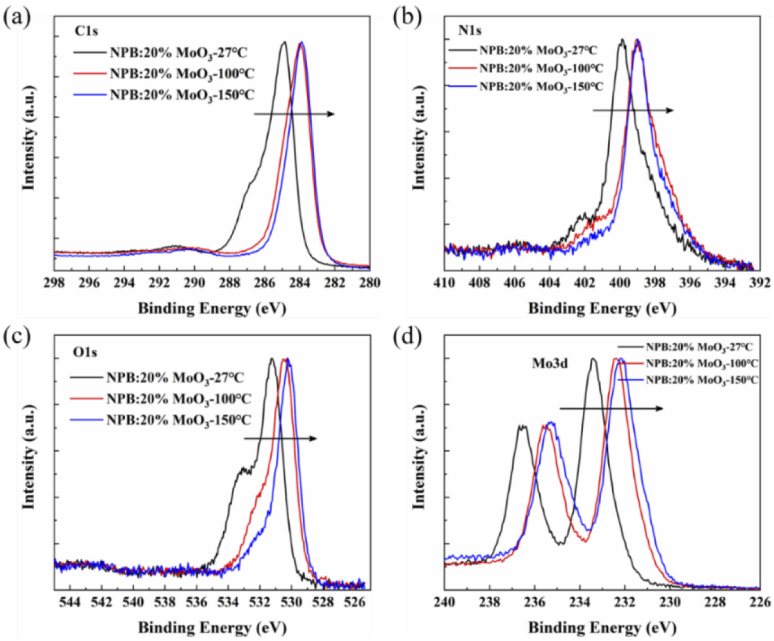

Fig. 4. XPS spectra of NPB: 20 vol% MoO_3 composite films annealed at different temperatures: (a) C 1s, (b) N 1s, (c) O 1s, (d) Mo 3d nuclear energy level spectra.

film. There is only a single valence Mo element in the film [24] when the thickness of the MoO_3 film is less than 15 nm. The binding energy measured at room temperature for hexavalent Mo $3d_{3/2}$ and Mo $3d_{5/2}$ are 236.65 and 232.4 eV, respectively. Compared with pure MoO_3 film with hexavalent Mo $3d_{3/2}$ and Mo $3d_{5/2}$, the binding energy of each valence state of MoO_3-doped NPB film exhibits an enhancement of around 1 eV. Meanwhile, the overall binding energy shifts to the direction of high binding energy. We speculate that it may be caused by the interaction between Mo element and NPB molecule, and a charge transfer complex is formed between MoO_3 and NPB [25]. The binding energy of each valence state and the comparison with pure MoO_3 film are presented in Table 1.

Table 1. The binding energy values of various oxidation states of Mo with NPB: 20 vol% MoO_3 at room temperature and the corresponding state values reported in the literature.

Peak	Valance	Binding energy (eV) (Experimentally measured)	MoO_3 film binding energy (eV) [26]
A	+6	236.65	235.6
A'	+6	233.53	232.4
B	+5	235.56	234.4
B'	+5	232.51	231.3
C	+4	233.82	233.0
C'	+4	230.75	229.8

After the composite film was annealed at 100 and 150 °C in the atmosphere, the measured Mo 3d patterns are illustrated in Fig. S4s(b) and (c). As is depicted in Fig. S4(b), Mo^{6+} and Mo^{5+} are present in the composite film after annealing at 100°C, while the Mo^{4+} containing in the film at room temperature has disappeared at this time. This is because after the film is annealed in air, the Mo^{4+} in the film is oxidized to the higher valence states of Mo^{6+} and Mo^{5+}. However, compared with the binding energy of Mo^{6+} and Mo^{5+} in the film at room temperature,

Optical Materials EXPRESS

the binding energy of Mo^{6+} and Mo^{5+} changes after annealing at 100°C, as the specific relevant data are shown in Table S1. After the cell is annealed at 100°C, the binding energies of Mo^{6+} and Mo^{5+} are reduced by 1 eV compared with Mo^{6+} and Mo^{5+} in the composite film at room temperature. The binding energies of Mo^{6+} $3d_{5/2}$ and Mo^{6+} $3d_{3/2}$ are 235.60 and 232.48 eV, respectively. This result is consistent with the binding energy of Mo^{6+} in the pure MoO_3 film. Apparently, the interaction between Mo^{6+}, Mo^{5+} and NPB molecules is destroyed after high temperature annealing at 100°C, and only separate Mo^{6+}, Mo^{5+} and NPB molecules exist.

Fig. S4(c) shows the orbital XPS energy spectrum of Mo element in the composite film after annealing at 150°C. The specific binding energy data are shown in Table S2. It can be seen from the figure that after annealing at 150°C, there is only a single Mo^{6+} in the composite film. After being annealed at 150°C, Mo^{5+} is further oxidized to Mo^{6+}. The binding energies of $3d_{5/2}$ and $3d_{3/2}$ are 235.30 eV and 232.14 eV, respectively, almost the same as that of Mo^{6+} in pure MoO_3 film.

According to the XPS analysis, it can be concluded that the MoO_3-doped NPB composite film prepared by the vacuum evaporation method contains charge transfer complexes, which prevents the heterogeneous nucleation of small organic molecules NPB and enhances the thermal stability of the composite film. The high-temperature annealing oxidizes the Mo in the composite film to form a high-valence state of Mo, which is beneficial to the transport of holes in the film.

In response to the above phenomenon, we make the following assumptions:

Under the same heating conditions, the energy received by the film per unit time per unit area is Q_1. For the neat NPB film, we suppose that the NPB molecule vibrates normally at a specific average frequency ω_1. Its vibration mode is q_1, $\hbar$=h/2π, where h is Planck's constant, as is shown in Fig. 5(a). Then,

$$Q_1 = \sum_{k=0}^{n} \hbar\omega_k q_k = \hbar\omega_1 q_1 \tag{1}$$

For the MoO_3-doped NPB composite film, MoO_3 will also gain a part of heat energy during the heat conduction process. Assuming that the average vibration frequencies of NPB molecules and MoO_3 molecules are ω_2 and ω_3, respectively, and their vibration modes are q_2 and q_3, respectively. Then,

$$Q_1 = \sum_{k=0}^{n} \hbar\omega_{2k} q_{2k} + \sum_{k=0}^{n} \hbar\omega_{3k} q_{3k} = \hbar\omega_2 q_2 + \hbar\omega_3 q_3 \tag{2}$$

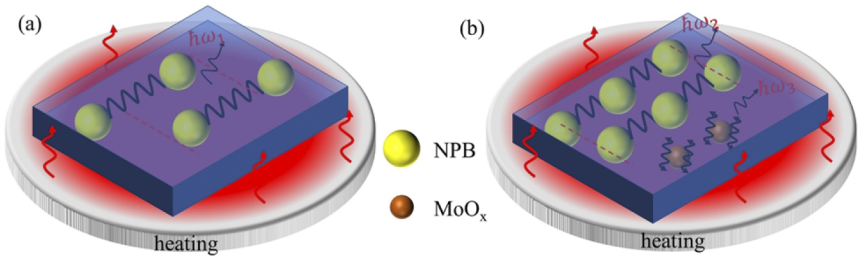

Fig. 5. The lattice vibration mechanism of (a) pure NPB and (b) MoO_x-doped NPB composite films at high temperature.

For the single NPB and MoO_x molecule in the neat film and composite film, assuming that the thermal energy received is Q_2, it can be inferred that ω_1=ω_2+ω_3, as shown in the following

Optical Materials EXPRESS

formula.

$$Q_2 = \hbar\omega_2 + \hbar\omega_3 = \hbar\omega_1 \tag{3}$$

That is, the molar mass of NPB is 588.74 g/mol, and the molar mass of MoO_3 is 143.94 g/mol. Because of the conservation of system energy, it can be inferred that $\omega_2 \ll \omega_3$, which can also be analogized to the entire thin film system. Compared with pure NPB film, the MoO_3 in the doped composite film will greatly absorb heat in the form of phonon emission. Therefore, the NPB lattice vibration frequency in the composite film decreases, and the phonon emission decreases. It is observed that the thermal energy damage to the NPB is lower with the mobility change decreasing, as shown in Fig. 5(b). The Mo: O ratio of the NPB doped MoO_3 composite film does not satisfy the stoichiometric ratio of MoO_3 at room temperature *via* the XPS analysis, yet after high temperature annealing, the Mo: O ratio gradually tends to be 1:3. This signifies that the molar mass of MoO_x is gradually increasing during the process from normal temperature to high temperature, which causes that part of the heat transfer to the NPB molecules, generating a slight increase on the current intensity of the hole-only cells prepared by the NPB doped MoO_3 composite film at high temperature.

On top of that, in order to determine the chemical behavior and composition of the Cs_2CO_3-doped TmPyPB composite film, XPS was applied to understand the diversification in the binding energy of different elements. The results measured are depicted in Fig. S5. As elaborated in Fig. S5(a), the C 1s binding energy of the composite film is the highest at room temperature. When the annealing temperature increases, the binding energies shift slightly to a lower binding energy. The C 1s binding energy of the composite film annealed at 100 °C recovers the standard binding energy (284.6 eV). It indicates that Cs_2CO_3-doping exerts a certain influence on the carbon bonds in TmPyPB. Meanwhile, the high temperature below 100 °C fails to completely destroy the interaction between them, which affects the stability of the composite film definitely. The XPS energy spectra corresponding to N 1s and O 1s exhibit no significant changes found in the binding energy in the composite film, as shown in Fig. S5s (b) and (c). The binding energy spectra of Cs $3d_{5/2}$ and Cs $3d_{3/2}$ in the composite film are described in Fig. S5(d). After high temperature treatment, the binding energy did not change obviously. It is worth noting that Duan *et al.* clarified the electron injection mechanism of thermal decomposition of Cs_2CO_3 using thermodynamic calculations, and concluded that Cs_2CO_3 decomposed into metal Cs instead of Cs_2O after high-temperature evaporation. In addition, the material in the deposited Cs_2CO_3 sample observed *via* XPS is consistent with the standard Cs metal [27]. Therefore, Cs is present in the Cs_2CO_3-doped TmPyPB composite film. The binding energy of Cs remains unchanged after high temperature treatment, indicating that the composite film can still maintain a steady state at high temperature.

As illustrated in Fig. 6(s) (a) and (b), it refers to the ultraviolet absorption spectra (ABS) and PLQYs of the NPB film after annealing at 27, 80, 100, and 150 °C for 30 min. After high temperature process, the ABS and PLQY spectra of the NPB film showed a downward trend. The absorption strength and PLQY of the NPB film dropped abruptly by nearly 40% especially at 150 °C. Compared with the ultraviolet absorption and PLQY of the film after annealing at 150°C, the annealing temperature has a greater impact on the film.

Figure S6 depicted the PLQYs of the TmPyPB film after annealing at 27, 80, 100, and 150°C for 30 min. After high temperature treatment, the PLQY of the TmPyPB film exhibited a downward trend, especially at 100°C, with the PLQY dropping by nearly 20%. These observations are coherent with the NPB film at different temperatures.

As shown in Fig. S7, the NPB films were annealed at 100°C for the time of 0, 15, 30, and 60 min. The roughness of the four films after annealing was 0.525, 0.487, 0.486, and 0.494 nm, respectively. Furthermore, a high-temperature ($>T_g$) treatment for a long time made the film become flatter since the film was at the stage of crystalize phase.

Optical Materials EXPRESS

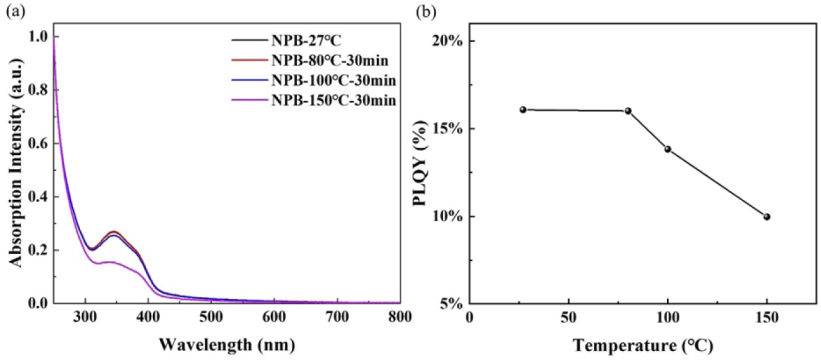

Fig. 6. (a) Ultraviolet absorption spectra of NPB thin films annealed at different temperatures for 30 min and (b) their PLQY curve.

3.2. *Electrical properties of MoO_x-doped organic hole-only cells*

It can be observed from Fig. 7(a) that the current intensity of the cell is the lowest at 80 °C. This may be due to the rough surface of the NPB film after the treatment of 80 °C (as shown in Fig. 2(b)). This is also related to the decrease of contact surface of the anode and cathode of the cell, and the reduction of charge carrier injection capacity. The current intensity of the cell increases at 100 °C, which is determined by the carrier transport characteristics of the amorphous organic material. It can be acquired that when the temperature increases, carriers can overcome the interface barrier, so that the current intensity of the cell also rises with the mobility of the material. As indicated in Fig. S8(a), the *I-V* curve of the electron-only cell containing neat TmPyPB indicates an unstable trend at different temperatures with the current intensity moving irregularly, which is not conducive to exploring the impact of high temperature. Nevertheless, another cell containing an EIL exhibits fine diode characteristics in Fig. S8(b). It could be attributed to the addition of LiF, causing the LiF/Al cathode to possess ohmic contact characteristics, which facilitates electron injection and contributes to stabilize the electrode interface. Consequently, in the subsequent comparative experiments, we select electron-only cells containing an EIL.

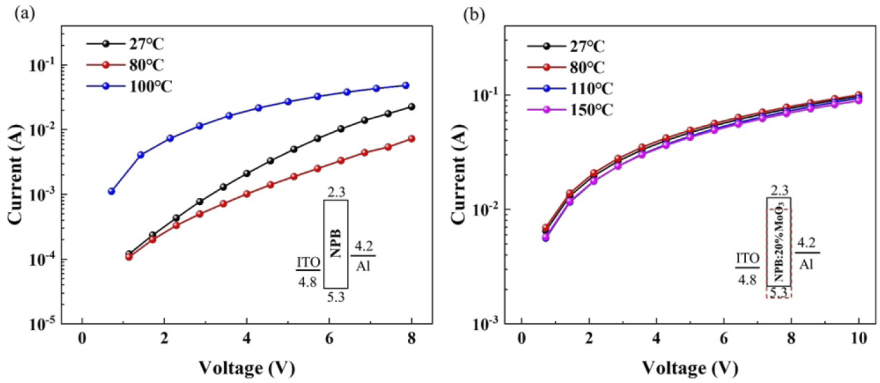

Fig. 7. *I-V* curves of hole-only cells with (a) NPB and (b) NPB : 20 vol% MoO_3 at different annealing temperatures.

As expected, the *I-V* curve of the cell based on NPB:20 vol% MoO_3 remains very stable regardless of high temperature, basically keeping the same with the normal temperature *I-V*

Optical Materials EXPRESS

curve, and the current intensity is only slightly enhanced. This further suggests that there is no crystallization phenomenon in the composite film and no obvious dependence on temperature. There has been previous report that the crystallization of the NPB layer is affected by whether the NPB layer faces the crystalline molecular layer or the amorphous molecular layer [28,29]. In the case of ITO/NPB: MoO_3, the charge transfer interaction, between the doped guest and the host, can change the surface energy of the doped layer and prevent the heterogeneous nucleation of organic molecules, thereby transforming the T_g of the organic material and increasing its thermal stability. As indicated in Fig. S9, the cell based on TmPyPB: 10 vol% Cs_2CO_3 exhibits high-temperature stability. Even at 100 °C, the current intensity of the cell still exhibits an increasing trend steadily without appearing the breakdown phenomenon. Simultaneously, the high temperature caused the Cs element to diffuse uniformly in the composite film, accordingly the film conductivity was enhanced. It predicts that the composite film still has excellent stability, after it is annealed at high temperature in the air, with the possibility to generate defects or even undergo crystallization, which rebounds to the stable operation of OLED at high temperature.

3.3. OLED device performance

Figure 8(s) (a) and (b) represents the current density-voltage-luminance (*J-V-L*) and current efficiency (CE)-luminance (*L*)-power efficiency (PE) characteristic curves, respectively, when the devices are annealed at 50 and 80°C. Figure 8(s) (c) and (d) presents the *J-V-L* and CE-*L*-PE characteristic curves, respectively, at the annealing temperature of 100°C. The experimental results confirm that the maximum CE of the device gradually decreases as the annealing temperature increases.

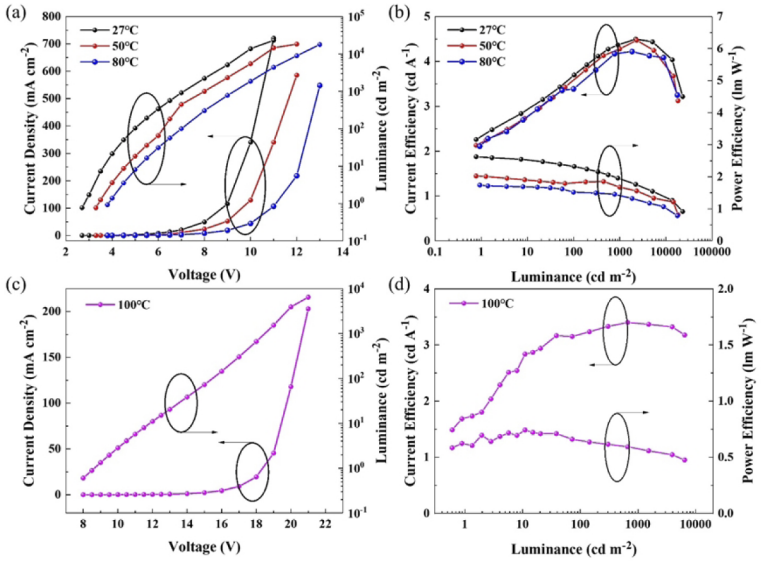

Fig. 8. (a) *J-V-L* diagram and (b) the CE-*L*-PE characteristic curves of Device A after annealing at 27, 50, and 80°C, respectively. (c) *J-V-L* diagram and (d) the CE-*L*-PE characteristic curves of Device A after annealing at 100°C.

As presented in Table 2, the turn-on voltage of the Device A is 2.9 V at room temperature, afterwards the turn-on voltage after high temperature annealing is 3.0, 3.0, and 5.8 V, respectively. Meanwhile, the maximum luminance of the corresponding device is 25500, 29900, 21400, and 9197 cd m^{-2}, respectively. The turn-on voltage does not increase significantly after annealing at a high temperature below 100°C, but it increases by two times after being annealed at 100°C.

Optical Materials EXPRESS

Under the identical driving voltage, the luminance and current density of the device after high temperature annealing are lower than that of the device under normal temperature environment, which reveals that the carrier mobility of the device after cooling decreases with the annealing temperature. This also demonstrates that some damage was caused to the organic materials inside the device because of the high temperature annealing. As listed in Table 2, the maximum CEs of Device A at different temperatures are 8.08, 7.90, 5.63, and 3.48 cd A^{-1}, respectively. Meanwhile, the maximum PEs are 8.75, 8.27, 5.89, and 0.95 lm W^{-1}, respectively. The result reveals that the CE after annealing at 80 °C is only half of that at room temperature, with the PE reduced by 27%, which is very unfavorable for the stable operation of OLEDs at high temperatures.

Table 2. Comparison of main performance parameters of Devices A and B at different annealing temperature

Temperature (°C)[a]	Devices	V_{on} [V][b]	$\eta_{c,max}$ (cd A^{-1})[c]	L_{max} (cd m^{-2})[d]	$\eta_{pe,max}$ (lm W^{-1})[e]
27°C	A B	2.9 2.9	8.08 8.22	25500 29630	8.75 8.90
50°C	A B	3.0 2.7	7.90 8.39	29900 34826	8.27 9.75
80°C	A B	3.0 2.8	5.63 7.29	21400 22396	5.89 8.18
100°C	A B	5.8 3.3	3.48 6.03	9197 21879	0.95 5.74

[a]Devices with different temperatures;
[b]Corresponding voltage when the device luminance is 1 cd m^{-2}
[c]Maximum CE;
[d]Maximum device luminous luminance;
[e]Maximum PE

The luminescence performance of Device B annealed at different temperatures for 30 min is depicted in Fig. 9. It can be surveyed from Fig. 9(a) that under the identical driving voltage, the luminance and current density from 27 to 80°C are higher than that of the device annealed at 27°C, which is completely different from the unoptimized device presenting in the previous experiment. At room temperature, the turn-on voltage of the device is 2.9 V, while the turn-on voltages are 2.7, 2.8, and 3.3 V at 50, 80 and 100°C, respectively. The turn-on voltage exhibits a small drop at 50 and 80°C, while it increases by 0.4 V at 100°C. The device luminance and current density decrease to a certain extent after the device is annealed at a high temperature of 100 °C. This is because the electron-transporting capacity of TmPyPB doped with Cs_2CO_3 is further enhanced after the high temperature annealing at 100 °C, while the hole-transporting capacity does not change significantly, resulting in carrier unbalance inside the device. Compared with Device A, the stability of Device B has been greatly improved. The CE-*L*-PE characteristic curves of the devices annealed at different temperatures are illustrated in Fig. 9(b). The results demonstrate that the performance of Device B remains the best after annealing at 50°C; meanwhile the CE and PE achieve the largest value. As depicted in Table 2, the maximum CEs of the device annealed at different temperatures are 8.22, 8.39, 7.29, and 6.03 cd A^{-1}, respectively, and the maximum PEs are 8.90, 9.75, 8.18, and 5.74 lm W^{-1}, respectively. After Device B is annealed at 80°C, the current efficiency drops by only 12%, and correspondingly the PE decreases only by 9%. The device performance still remains excellent even at a high temperature of 100°C.

3.4. Endurance testing

The normalized luminance decay curve of Device A with lifetime is depicted in Fig. 10(a). The T_{50} (the time of the brightness dropping to half of the initial luminance) of the device lifetime after annealing temperature of 27, 50, 80, and 100°C, are 87, 71, 40, and 30 h, respectively. The annealed device at 50 °C exhibits more reduced decay characteristics than that at room temperature in the first 50 hours. The device annealed at 100°C is more severely damaged with the luminance dropping sharply after 19 h, which indicates that high temperature will cause

Optical Materials EXPRESS

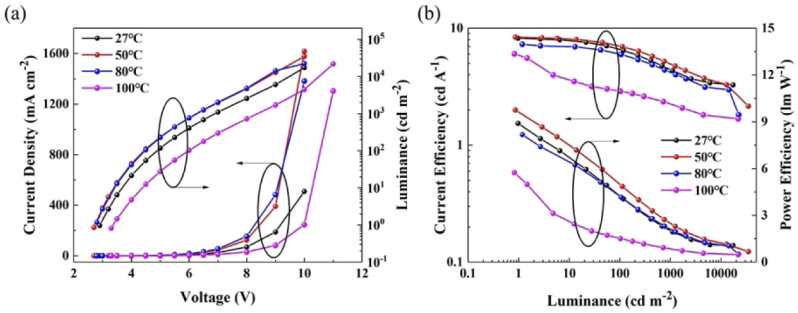

Fig. 9. (a) The *J*-*V*-*L* curves and (b) the CE-*L*-PE curves of Device B after annealing at 27, 50, 80, and 100°C.

great damage to the stability of OLED devices. As presented in Fig. 10(b), the T_{50} of the device lifetime after annealing temperature of 27, 50, 80, and 100°C, reach 143, 125, 208, and 74 h, respectively. At all annealing temperatures, the device luminance curve with time exhibits a rapid decline in the early stage, which is consistent with the characteristics of the conventional device lifetime curve [30,31]. Among them, the device annealed at 80 °C presents the most excellent device lifetime. This is because that OLED is a current-driving device whose life is affected by the amount of charge passed. Furthermore, it is inversely proportional to the driving current within a certain range. However, the current of the device after annealing is smaller than that at room temperature. Therefore, the lifetime of the device is strengthened after high temperature annealing at 80 °C. Compared with Device A, the device lifetime has been greatly enhanced, which proves that the doped device can reduce the interface barrier between interlayers and improve the thermal stability of the low T_g organic compounds, realizing the stable operation of OLEDs at high temperatures.

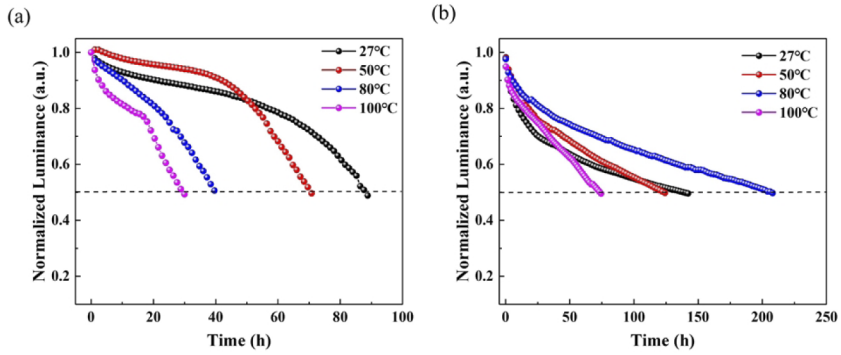

Fig. 10. Normalized luminance decay curve with time of (a) Device A and (b) Device B. Initial luminance is 1000 cd m^{-2}.

4. Conclusion

In summary, we have mainly investigated the failure mechanism of organic thin films and devices in high-temperature environments, and proposed an optimization scheme for low-T_g organic thin film to improve their thermal stability. First, we have studied the photophysical properties of the carrier transport layer in OLED devices after high-temperature annealing. Through the AFM characterization, it was observed that the surface roughness of the low-T_g NPB was significantly increased when being annealed at 50 and 80 °C, respectively. The reason for the difference could

Optical Materials EXPRESS

be attributed to the agglomeration and the beginning of microcrystals on the surface of the low-T_g organic materials after annealing in the air. On the other hand, the composite films, both the MoO_3-doped NPB film and Cs_2CO_3-doped TmPyPB film exhibit superior thermal stability in terms of surface morphology and electrical properties.

Finally, the influence of high temperature annealing on the optical performance and stability of OLED devices was investigated. The results revealed that the current density, luminance and efficiency of the device gradually decreased with the annealing temperature. On the contrary, the current density and luminance of the doped device are improved to a certain extent after being annealed at 50 and 80 °C, respectively. The CE of the device is only reduced by 12% after annealing at 80°C, meanwhile the lifetime reaching 208 h is the longest among those of the devices. Nevertheless, the CE of the undoped comparative device dropped by nearly 30% with the lifetime reaching 40 h. Accordingly, the thermal stability of the devices can be greatly strengthened by optimized doping engineering.

Funding. Science and Technology Commission of Shanghai Municipality (17DZ2281700, 19DZ2281000); National Natural Science Foundation of China (11974236, 61775130).

Acknowledgements. This work was financially supported by the National Natural Science Foundation of China (61775130, 11974236) and the Science and Technology Commission of Shanghai Municipality Program (19DZ2281000; 17DZ2281700).

Disclosures. The authors declare no conflicts of interest.

Data availability. No data were generated or analyzed in the presented research.

Supplemental document. See Supplement 1 for supporting content.

References

1. M. Mao, T. L. Lam, W. P. To, X. Lao, W. Liu, S. Xu, G. Cheng, and C. M. Che, "Stable, 5with a single tetradentate platinum(ii) emitter having long operational lifetime," Adv. Mater. **33**(2), 2004873 (2021).
2. J. Yao, W. Liu, C. Lin, Q. Sun, Y. Dai, X. Qiao, D. Yang, J. Chen, and D. Ma, "High efficiency and long lifetime fluorescent white organic light-emitting diodes by phosphor sensitization to strategically manage singlet and triplet excitons," J. Mater. Chem. C **9**(10), 3626–3634 (2021).
3. Y. J. Yu, X. Q. Wang, J. F. Liu, Z. Q. Jiang, and L. S. Liao, "Harvesting triplet excitons for near-infrared electroluminescence via thermally activated delayed fluorescence channel," iScience **24**(2), 102123 (2021).
4. Y. Lin, K. Guo, Z. Gao, H. Wang, C. Li, T. Xu, and B. Wei, "Photoluminescence characteristics of organic molecules in the accelerated aging organic light-emitting diodes," Phys. Status Solidi A **210**(12), 2716–2719 (2013).
5. S. Shahnawaz, S. Sudheendran Swayamprabha, M. R. Nagar, R. A. K. Yadav, S. Gull, D. K. Dubey, and J.-H. Jou, "Hole-transporting materials for organic light-emitting diodes: an overview," J. Mater. Chem. C **7**(24), 7144–7158 (2019).
6. D. H. Chung, S. W. Hur, S. K. Kim, J. U. Lee, C. H. Kim, J. W. Hong, and T. W. Kim, "Temperature-dependent electrical properties of organic light-emitting diodes depending on cathodes," Curr. Appl. Phys. **4**(6), 667–670 (2004).
7. J. A. McEwan, A. J. Clulow, A. Nelson, N. R. Yepuri, P. L. Burn, and I. R. Gentle, "Dependence of organic interlayer diffusion on glass-transition temperature in OLEDs," ACS Appl. Mater. Interfaces **9**(16), 14153–14161 (2017).
8. G. Nenna, G. Flaminio, T. Fasolino, C. Minarini, R. Miscioscia, D. Palumbo, and M. Pellegrino, "A study on thermal degradation of organic LEDs using IR imaging," Macromol. Symp. **247**(1), 326–332 (2007).
9. S. W. Yin, Z. Shuai, and Y. l. Wang, "A quantitative structure-property relationship study of the glass transition temperature of OLED materials," J. Chem. Inf. Comput. Sci. **43**(3), 970–977 (2003).
10. A. R. G. Smith, J. L. Ruggles, H. Cavaye, P. E. Shaw, T. A. Darwish, M. James, I. R. Gentle, and P. L. Burn, "Investigating Morphology and Stability of Fac-tris (2-phenylpyridyl)iridium(III) Films for OLEDs," Adv. Funct. Mater. **21**(12), 2225–2231 (2011).
11. M. Carrarda, S. Goncalves-Contoa, L. Si-Ahmeda, D. AdeÁsb, and A. Sioveb, "Improved stability of interfaces in organic light emitting diodes with high Tg materials and self-assembled monolayers," Thin Solid Films **352**(1-2), 189–194 (1999).
12. H. Y. Cho, L. S. Park, Y. S. Han, Y. Kwon, and J.-Y. Ham, "High-TgN-triarylamine derivatives as a hole injecting layer in organic light-emitting diodes," Mol. Cryst. Liq. Cryst. **499**(1), 323–332 (2009).
13. Z. Bin, G. Dong, P. Wei, Z. Liu, D. Zhang, R. Su, Y. Qiu, and L. Duan, "Making silver a stronger n-dopant than cesium via in situ coordination reaction for organic electronics," Nat. Commun. **10**(1), 866 (2019).
14. K. Guo, C. Si, C. Han, S. Pan, G. Chen, Y. Zheng, W. Zhu, J. Zhang, C. Sun, and B. Wei, "High-performance flexible inverted organic light-emitting diodes by exploiting MoS_2 nanopillar arrays as electron-injecting and light-coupling layers," Nanoscale **9**(38), 14602–14611 (2017).

Optical Materials EXPRESS

15. C.-M. Keum, N. M. Kronenberg, C. Murawski, K. Yoshida, Y. Deng, C. Berz, W. Li, M. Wei, I. D. W. Samuel, and M. C. Gather, "The role of metallic dopants in improving the thermal stability of the electron transport layer in organic light-emitting diodes," Adv. Opt. Mater. **6**(17), 1800496 (2018).
16. Y. Kwon, S. H. Han, S. Yu, J. Y. Lee, and K. M. Lee, "Functionalized phenylimidazole-based facial-homoleptic iridium(iii) complexes and their excellent performance in blue phosphorescent organic light-emitting diodes," J. Mater. Chem. C **6**(16), 4565–4572 (2018).
17. D. Saito, H. Sasabe, T. Kikuchi, T. Ito, H. Tsuneyama, and J. Kido, "Improved operational lifetime of deep-red phosphorescent organic light-emitting diodes using a benzothienobenzothiophene (BTBT)-based p-type host material," J. Mater. Chem. C **9**(4), 1215–1220 (2021).
18. X. Zhou, J. Blochwitz, M. Pfeiffer, A. Nollau, T. Fritz, and K. Leo, "Enhanced hole injection into amorphous hole-transport layers of organic light-emitting diodes using controlled p-Type doping," Adv. Funct. Mater. **11**(4), 310–314 (2001).
19. M. Ashrafi, H. Fakhraian, and M. A. Dehnavi, "Synthesis, characterization and properties of nitropolybutadiene as energetic plasticizer for NHTPB Binder," Propellants, Explos. Pyrotech. **42**(3), 269–275 (2017).
20. Z. Li, Z. Wu, W. Fu, D. Wang, P. Liu, B. Jiao, X. Lei, G. Zhou, and Y. Hao, "Stable amorphous bis(diarylamino)biphenyl derivatives as hole-transporting materials in OLEDs," Electron. Mater. Lett. **9**(5), 655–661 (2013).
21. M. S. Xu, J. B. Xu, and J. An, "Visualization of thermally activated morphology evolution of N, N'-di(naphthalene-1-yl)- N, N'-diphthalbenzidine films on ITO/copper phthalocyanine underlying layer," Appl. Phys. A: Mater. Sci. Process. **81**(6), 1151–1156 (2005).
22. Z.Q. Gao, W.Y. Lai, T.C. Wong, C.S. Lee, I. Bello, and S.T. Lee, "Organic electroluminescent devices by high-temperature processing and crystalline hole transporting layer," Appl. Phys. Lett. **74**(22), 3269–3271 (1999).
23. A. A. Bolzan, B. J. Kenned, and C. J. Howard, "Neutron Powder Diffraction Study of Molybdenum and Tungsten Dioxides," Aust. J. Chem. **48**(8), 1473–1477 (1995).
24. K. Kanai, K. Koizumi, S. Ouchi, Y. Tsukamoto, K. Sakanoue, Y. Ouchi, and K. Seki, "Electronic structure of anode interface with molybdenum oxide buffer layer," Org. Electron. **11**(2), 188–194 (2010).
25. B. Tian, D. Ban, and H. Aziz, "Enhanced bulk conductivity and bipolar transport in mixtures of MoOx and organic hole transport materials," Thin Solid Films **536**, 202–205 (2013).
26. T. S. Sian and G. B. Reddy, "Optical, structural and photoelectron spectroscopic studies on amorphous and crystalline molybdenum oxide thin films," Sol. Energy Mater. Sol. Cells **82**(3), 375–386 (2004).
27. Q. Liu, L. Duan, Y. Li, J. Qiao, Z. Yu, D. Zhang, L. Wang, G. Dong, and Y. Qiu, "Study on the electron injection mechanism of thermally decomposable Cs_2CO_3," Jpn. J. Appl. Phys. **48**(10), 102302 (2009).
28. F. Wang, X. Qiao, T. Xiong, and D. Ma, "The role of molybdenum oxide as anode interfacial modification in the improvement of efficiency and stability in organic light-emitting diodes," Org. Electron. **9**(6), 985–993 (2008).
29. I. Zhivkov, E. Spassova, G. Danev, S. Andreev, and T. Ivanov, "Vacuum deposited copper phthalocyanine thin films—structure and surface morphology," Vacuum **51**(2), 189–192 (1998).
30. M. S. Weaver, L. A. Michalski, K. Rajan, M. A. Rothman, J. A. Silvernail, J. J. Brown, P. E. Burrows, G. L. Graff, M. E. Gross, P. M. Martin, M. Hall, E. Mast, C. Bonham, W. Bennett, and M. Zumhoff, "Organic light-emitting devices with extended operating lifetimes on plastic substrates," Appl. Phys. Lett. **81**(16), 2929–2931 (2002).
31. J. Zhang, W. Li, G. Cheng, X. Chen, H. Wu, and M. H. Herman Shen, "Life prediction of OLED for constant-stress accelerated degradation tests using luminance decaying model," J. Lumin. **154**, 491–495 (2014).

158.132.181.240 on 2023-06-16 04:03:11